

A search for distant radio galaxies from SUMSS and NVSS: II. Optical Spectroscopy^{*}.

Carlos De Breuck¹, Ilana Klammer², Helen Johnston², Richard W. Hunstead², Julia Bryant², Brigitte Rocca-Volmerange³, Elaine M. Sadler²

¹ *European Southern Observatory, Karl Schwarzschild Straße 2, D-85748 Garching, Germany.*

² *School of Physics, University of Sydney, Sydney NSW 2006, Australia.*

³ *Institut d'Astrophysique de Paris, UMR7095 CNRS, Université Pierre & Marie Curie, 98 bis Boulevard Arago, 75014 Paris, France.*

5 February 2008

ABSTRACT

This is the second in a series of papers presenting observations and results for a sample of 76 ultra-steep-spectrum (USS) radio sources in the southern hemisphere designed to find galaxies at high redshift. Here we focus on the optical spectroscopy program for 53 galaxies in the sample. We report 35 spectroscopic redshifts, based on observations with the Very Large Telescope (VLT), the New Technology Telescope (NTT) and the Australian National University's 2.3m telescope; they include five radio galaxies with $z > 3$. Spectroscopic redshifts for the remaining 18 galaxies could not be confirmed: three are occulted by Galactic stars, eight show continuum emission but no discernible spectral lines, whilst the remaining seven galaxies are undetected in medium-deep VLT integrations. The latter are either at very high redshift ($z \gtrsim 7$) or heavily obscured by dust. A discussion of the efficiency of the USS technique is presented. Based on the similar space density of $z > 3$ radio galaxies in our sample compared with other USS-selected samples, we argue that USS selection at 843–1400 MHz is an efficient and reliable technique for finding distant radio galaxies.

Key words:

surveys – radio continuum: general – radio continuum: galaxies – galaxies: active – galaxies: high-redshift

1 INTRODUCTION

A key requirement of structure formation models is being able to predict the abundance of massive galaxies at high redshift. This has been a problem for hierarchical galaxy formation models within the framework of a Lambda cold dark matter (Λ CDM) cosmogony (*e.g.* White & Frenk 1991). These models predict that massive systems assemble via mergers and coalescence of smaller, intermediate-mass discs (*e.g.* Cole 1991; Kauffmann et al. 1993; Baugh et al. 1996; Kauffmann et al. 1999a). However, the predicted decline in abundance of early-type galaxies above $z = 1.5$ (Kauffmann et al. 1999b; Devriendt & Guiderdoni 2000), which is a crucial test of these models, fails to reproduce the observations at high redshift. The abundance of mas-

sive ($\sim 10^{12} M_{\odot}$) sub-millimetre galaxies with high star-formation rates ($\sim 10^3 M_{\odot} \text{ yr}^{-1}$) at $z > 2$ (Ivison et al. 2002; Chapman et al. 2003) is at odds with hierarchical formation. So too is the existence of massive old elliptical galaxies beyond $z = 1.5$ which have been selected in the radio or near-IR (Dunlop et al. 1996; Daddi et al. 2000; Cimatti et al. 2004), and the massive ($M_{\text{baryonic}} = 10^{12} M_{\odot}$; Rocca-Volmerange et al. 2004) hosts of $z > 3$ radio galaxies containing large reservoirs ($\sim 10^{11} M_{\odot}$) of molecular gas and dust (Stevens et al. 2003; Papadopoulos et al. 2000; De Breuck et al. 2003; Klammer et al. 2005).

These observations have led to renewed consideration of alternative galaxy formation models, such as the ‘downsizing’ idea where the most massive galaxies form earliest in the Universe, and star formation activity is progressively shifted to smaller systems (*e.g.* Cowie et al. 1996; Kodama et al. 2004; Treu et al. 2005). They have also prompted revisions of hierarchical formation models by adding new ingredients and assumptions. Many models invoke feedback by supernovae, starbursts or active galac-

^{*} Based on observations obtained with the European Southern Observatory, Paranal and La Silla, Chile (Programs 72.A-0259 and 073.A-0348) and the Australian National University 2.3m telescope

tic nuclei (AGN) (*e.g.* Granato et al. 2004; Croton et al. 2005), while others abandon a universal initial mass function and consider a full radiative treatment of dust (Baugh et al. 2005). Several authors have also emphasised the importance of feedback due to powerful radio jets, which may push back and heat the ionized gas, reducing or even stopping the cooling flows building up the galaxy (Rawlings & Jarvis 2004; Croton et al. 2005). On the other hand, radio jets could also induce star formation (Rees 1989; Fragile et al. 2004; Klammer et al. 2004), as observed in at least one high redshift radio galaxy (Dey et al. 1997; Bicknell et al. 2000).

It is clear that observations of a large number of high redshift galaxies, in particular the most massive ones, are essential in order to constrain the structure formation models described above. Radio galaxies are known to be among the most massive galaxies known at each redshift (*e.g.* De Breuck et al. 2002; Rocca-Volmerange et al. 2004), and are ideal laboratories for studying the ‘radio feedback’ mechanism described above. Modern radio surveys cover almost the entire sky, and allow us to pinpoint the most extreme (*e.g.* the most massive) galaxies, provided one can isolate them in radio catalogues containing up to 2 million sources. We have started such a search for distant radio galaxies in the southern hemisphere using the 843 MHz Sydney University Molonglo Sky Survey (SUMSS; Bock, Large, & Sadler 1999) and the NRAO VLA Sky Survey (NVSS; Condon et al. 1998). In the first paper of this series (paper I; De Breuck et al. 2004), we define a sample of 76 high redshift radio galaxy candidates selected on the basis of their ultra-steep radio spectra (USS; $\alpha \leq -1.3$, $S_\nu \propto \nu^\alpha$), which has been almost the sole way to find $z > 3$ radio galaxies (*e.g.* Röttgering et al. 1997; De Breuck et al. 2001; Jarvis et al. 2001). We also present high-resolution radio imaging to obtain accurate positions and morphological information, and near-IR identifications of the host galaxies. In this paper II, we present the results to date of optical spectroscopy to determine their redshifts. Multi-frequency radio observations and a discussion of the physics of ultra-steep-spectrum radio galaxies will be presented in a future paper (Klammer et al. in prep.). Throughout this paper, we adopt a flat Λ CDM cosmology with $H_0 = 71 \text{ km s}^{-1} \text{ Mpc}^{-1}$, $\Omega_M = 0.27$ and $\Omega_\Lambda = 0.73$ (Spergel et al. 2003).

2 OBSERVATIONS AND DATA REDUCTION

We used four different imaging spectrographs for the follow-up observations of the sources in our USS sample. For identifications detected on the digitised sky surveys or in the 2 Micron All Sky Survey (2MASS; Cutri et al. 2003), we used the Australian National University’s 2.3m telescope at Siding Spring Observatory, Coonabarabran, NSW with the Double Beam Spectrograph (DBS; Rodgers et al. 1988). For the remaining sources with $K \lesssim 19$ identifications, we initially attempted to measure redshifts with the ESO Multi-Mode Instrument (EMMI) on the New Technology Telescope (NTT). If no redshift could be determined, they were re-observed with the ESO Very Large Telescope (VLT), along with the faintest $K \gtrsim 19$ identifications, using the FOcal Reducer and Spectrographs (FORs; Appenzeller et al. 1997) on two of the unit telescopes.

We selected all our targets from the list of 76 USS

Table 1. Journal of the FORS2 *I*–band imaging (4'' apertures)

Source	t_{exp} s	<i>I</i> mag	<i>K</i> mag	Seeing ''
NVSS J002415–324102	600	23.7±0.2	19.5±0.4	0.5
NVSS J204420–334948	1620	>24.8	>21	0.8
NVSS J230035–363410	1500	>25	19.8±0.3	0.6
NVSS J230527–360534	1440	>25	>20.6	0.6
NVSS J231144–362215	1620	25.2±0.4	20.2±0.7	0.7
NVSS J231727–352606	1620	24.6±0.3	>20.6	0.8
NVSS J232100–360223	480	23.7±0.3	20.0±0.4	0.6
NVSS J232219–355816	1440	>25	>20.6	0.8
NVSS J234137–342230	1440	>25	>21	0.6
NVSS J235137–362632	1620	>25	>20.4	1.0

sources defined in paper I. Our goal was to obtain redshift information for the entire sample, but due to adverse weather conditions (mainly at the NTT), we could only observe 53 sources. Within the available RA range, we gave priority to the 53 sources in the sample with $\alpha < -1.3$. In total, we have observed 41 out of 53 sources with $\alpha < -1.3$ and 12 out of 23 sources with $\alpha > -1.3$. Our spectroscopic sample is thus 77% complete for the most important subset of $\alpha < -1.3$ sources.

2.1 *I*–band imaging

Before attempting optical spectroscopy of the 10 faintest *K*–band sources, we first imaged these fields in *I*–band using FORS2 on the VLT (see Table 1). We split the observations in exposures of typically 3 minutes each, while dithering the frames by a few arcseconds to ensure the object did not fall on a bad pixel on the detector. The pixel scale of FORS2 is 0''.25/pix, and the seeing during the observations varied between 0''.5 and 1''.0. We used the standard imaging reduction steps in *IRAF*, consisting of bias subtraction, flatfielding, and registration of the dithered frames. We fine-tuned the astrometry using all non-saturated 2MASS stars (typically ~ 10 per field) present in the images, yielding a solution which we estimate to be accurate up to $\sim 0''.3$, which is sufficient to identify the host galaxies of the radio sources. Finally, we measured the magnitudes in 4'' diameter apertures using the *IRAF* task *phot*.

2.2 Spectroscopy

Table 2 gives a journal of our spectroscopic observations. If a candidate was observed at different telescopes, we use only the best quality spectrum. The columns are:

- (1) Name of the source in IAU J2000 format.
- (2) *K*–band magnitude measured with a 64 kpc metric aperture. For objects without a redshift we adopted the 8''-aperture magnitudes from Paper I.
- (3) Spectroscopic redshift. Sources where no optical emission was detected over the entire wavelength range are marked by ‘undetected’. Sources where continuum emission was detected, but with no discernible features (emission/absorption lines or clear continuum breaks), are marked by ‘continuum’.

Table 2. Journal of the spectroscopic observations

(1) Source	(2) K (64 kpc) mag	(3) z	(4) ID [†]	(5) $\text{Log}(L_3)^{**}$	(6) Instr. [‡]	(7) t_{exp} s	(8) Slit PA °	(9) Extraction '' × ''	(10) RA(J2000) h m s	(11) DEC(J2000) ° ' ''
NVSS J001339–322445*	13.01	0.2598±0.0003	RG	25.12	2dFGRS	survey	...	2'' fibre	00 13 39.15	−32 24 43.9
NVSS J002001–333408	17.83	continuum	...	<26.6	EMMI	2400	345	1.0×1.0	00 20 01.14	−33 34 07.2
NVSS J002112–321208	19.06	undetected	FORS2	2400	0	...	00 21 12.40	−32 12 10.1
		undetected	FORS1	1800	0	...	00 21 12.56	−32 12 08.6
NVSS J002131–342225	15.19	0.249±0.001	RG	24.06	EMMI	1800	206	2.0×2.8	00 21 31.31	−34 22 22.6
NVSS J002219–360728	>14.12	0.364±0.001	RG	24.43	DBS	4000	90	2.0×9.1	00 22 19.50	−36 07 29.5
NVSS J002402–325253	18.98	2.043±0.002	RG	26.89	FORS1	1500	0	1.0×3.2	00 24 02.30	−32 52 54.7
NVSS J002415–324102	18.84	continuum	...	<27.0	FORS2	600	0	1.0×1.5	00 24 15.09	−32 41 02.4
NVSS J002427–325135	17.71	continuum	...	<27.1	EMMI	2400	359	1.0×4.3	00 24 27.72	−32 51 35.5
NVSS J002627–323653	>14.12	0.43±0.01	RG	25.01	DBS	4000	70	2.0×2.7	00 26 27.87	−32 36 52.4
NVSS J011032–335445	18.19	continuum	...	<26.6	EMMI	4000	332	1.5×1.2	01 10 31.99	−33 54 42.7
NVSS J011606–331241	18.00	0.352±0.001	RG	24.49	FORS1	1200	0	1.0×2.4	01 16 06.76	−33 12 43.0
NVSS J012904–324815*	12.58	0.180±0.001	RG	24.15	DBS	2400	235	2.0×4.6	01 29 04.26	−32 48 13.2
		0.1802±0.0003	RG	24.15	2dFGRS	survey	...	2'' fibre	01 29 04.29	−32 48 13.7
NVSS J015223–333833	17.99	undetected	FORS2	2160	0	...	01 52 22.93	−33 38 36.2
NVSS J015232–333952	16.19	0.618±0.001	RG	26.23	DBS	2400	0	2.0×9.1	01 52 32.42	−33 39 55.4
NVSS J015324–334117*	14.12	0.1525±0.0004	RG	23.70	2dFGRS	survey	...	2'' fibre	01 53 24.96	−33 41 25.4
NVSS J015418–330150*	19.81	undetected	FORS1	3600	0	...	01 54 18.26	−33 01 51.0
NVSS J015544–330633*	16.94	1.048±0.002	Q	26.03	EMMI	1800	206	2.0×2.3	01 55 44.61	−33 06 34.9
NVSS J021308–322338	19.43	3.976±0.001	RG	27.50	FORS1	2100	0	1.0×1.6	02 13 07.98	−32 23 39.9
NVSS J021716–325121	18.42	1.384±0.002	RG	26.11	FORS2	1800	0	1.0×1.5	02 17 15.92	−32 51 21.3
NVSS J030639–330432	17.78	1.201±0.001	RG	26.03	EMMI	500	268	2.0×2.6	03 06 39.77	−33 04 32.5
NVSS J202026–372823	18.11	1.431±0.001	RG	26.36	EMMI	3600	11	1.0×1.7	20 20 26.98	−37 28 21.0
NVSS J202140–373942	15.09	0.185±0.001	RG	23.85	EMMI	1800	169	1.0×1.0	20 21 40.59	−37 39 40.2
NVSS J202518–355834	18.21	undetected	FORS1	2400	0, 306	1.0×1.6	20 25 18.38	−35 58 32.3
NVSS J202856–353709*	16.58	0.000	S	...	EMMI	3600	169	2.0×1.8	20 28 56.77	−35 37 06.0
NVSS J202945–344812*	17.34	1.497±0.002	Q	26.57	EMMI	2400	177	2.0×2.1	20 29 45.82	−34 48 15.5
NVSS J204147–331731	16.86	0.871±0.001	RG	25.44	EMMI	3000	175	1.0×1.1	20 41 47.61	−33 17 29.9
NVSS J204420–334948	>21	undetected	FORS2	3600	0	...	20 44 20.83	−33 49 50.6
		undetected	FORS1	8100	0	...	20 44 20.83	−33 49 50.6
NVSS J213510–333703	18.58	2.518±0.001	RG	26.84	FORS1	3600	0	1.0×7.2	21 35 10.48	−33 37 04.4
NVSS J225719–343954	16.48	0.726±0.001	RG	25.55	EMMI	900	168	1.0×1.6	22 57 19.63	−34 39 54.6
NVSS J230123–364656	19.00	3.220±0.002	RG	27.13	FORS1	1800	0	1.0×1.6	23 01 23.54	−36 46 56.1
NVSS J230203–340932	18.60	1.159±0.001	RG	25.73	EMMI	3200	172	1.5×2.7	23 02 03.00	−34 09 33.5
NVSS J230404–372450*	17.23	continuum	...	<26.9	EMMI	3600	320	1.5×0.9	23 04 03.87	−37 24 48.0
NVSS J230527–360534	>20.6	undetected	FORS2	3600	0	...	23 05 27.63	−36 05 34.6
NVSS J230822–325027	18.55	0.000	S	...	EMMI	2000	170	2.0×0.9	23 08 46.72	−33 48 12.3
NVSS J231016–363624	14.57	0.000	S	...	DBS	2400	90	2.0×9.1	23 10 16.89	−36 36 33.1
NVSS J231144–362215	20.08	2.531±0.002	RG	26.72	FORS2	1800	0	1.0×2.0	23 11 45.22	−36 22 15.4
NVSS J231229–371324	17.53	continuum	...	<26.7	EMMI	2700	269	1.5×0.9	23 12 29.09	−37 13 25.8
NVSS J231317–352133	18.69	undetected	EMMI	3600	184	...	23 13 17.53	−35 21 33.6
NVSS J231338–362708	19.24	1.838±0.002	RG	26.33	FORS1	7200	123	1.0×4.0	23 13 38.37	−36 27 09.0
NVSS J231341–372504*	16.97	continuum	...	<26.5	EMMI	2400	347	1.5×1.3	23 13 41.67	−37 25 01.6
NVSS J231357–372413	16.53	1.393±0.001	RG	26.35	EMMI	1200	330	1.5×1.1	23 13 57.42	−37 24 15.6
NVSS J231402–372925	18.60	3.450±0.005	RG	27.95	FORS1	8100	0	1.0×1.6	23 14 02.40	−37 29 27.3
NVSS J231519–342710	17.91	0.970±0.001	RG	25.69	EMMI	5400	193	1.5×1.3	23 15 19.52	−34 27 13.3
NVSS J231727–352606	>20.58	3.874±0.002	RG	27.73	FORS2	3600	0	1.0×2.5	23 17 27.41	−35 26 07.1
NVSS J232001–363246	19.93	1.483±0.002	RG	26.11	FORS2	2400	0	1.0×1.5	23 20 01.27	−36 32 46.5
NVSS J232100–360223	19.47	3.320±0.005	RG	27.09	FORS2	1300	0	1.0×2.0	23 21 00.64	−36 02 24.8
NVSS J232322–345250*	17.12	continuum	...	<26.6	EMMI	3600	197	2.0×0.9	23 23 22.95	−34 52 49.0
NVSS J232408–353547	13.28	0.2011±0.0004	RG	23.86	2dFGRS	survey	...	2'' fibre	23 24 08.60	−35 35 45.2
NVSS J232602–350321*	14.56	0.293±0.001	RG	24.34	DBS	5400	285	2.0×3.6	23 26 01.67	−35 03 27.5
NVSS J232651–370909	19.28	2.357±0.003	RG	26.94	FORS1	1800	0	1.0×6.0	23 26 51.46	−37 09 10.7
NVSS J233558–362236*	16.67	0.791±0.001	RG	25.46	EMMI	3600	262	2.0×2.3	23 35 59.01	−36 22 41.6
NVSS J234145–350624	16.81	0.644±0.001	RG	27.14	DBS	1500	0	2.0×9.1	23 41 45.85	−35 06 22.2
NVSS J234904–362451	17.65	1.520±0.003	Q	26.53	EMMI	1800	329	1.0×1.2	23 49 04.26	−36 24 53.3

* These sources do not meet our USS criterion of $\alpha \leq -1.3$ (see paper I)

† RG = Radio Galaxy; Q = Quasar; S = Star.

** L_3 is the radio luminosity at 3 GHz in units of W/Hz. For ‘continuum’ sources, the upper limit is given for $z = 2.3$.

‡ 2dFGRS = 2-degree-field galaxy redshift survey (2dFGRS; Colless et al. 2001); EMMI = NTT/EMMI; FORS1 = VLT/FORS1; FORS2 = VLT/FORS2; DBS = ANU 2.3m/DBS

(4) The type of object detected (Radio Galaxy, Quasar or Star).

(5) The radio luminosity at a rest-frame frequency of 3 GHz, calculated using the 843 MHz and 1.4 GHz flux densities given in paper I.

(6) The instrument used to obtain the spectrum. Redshifts for three galaxies were obtained from the 2-degree-field galaxy redshift survey (2dFGRS; Colless et al. 2001).

(7) The total integration time.

(8) The position angle of the spectroscopic slit on the sky, measured North through East.

(9) The extraction width of the spectroscopic aperture. For the 2dFGRS, this is the fibre diameter. For all other galaxies, the first value is the slit width, and the second is the width of the extraction along the slit.

(10–11) The J2000 coordinates of the object centred in the spectroscopic slit.

2.3 ANU 2.3m

The 2.3m spectroscopy was carried out on 2003 August 1 to 3. To maximise the throughput, we replaced the dichroic beamsplitter with a plane mirror so that all the light was sent into the blue arm of the spectrograph. The detector was a coated SiTe 1752×532 pixel CCD with a spatial scale of $0''.91/\text{pix}$. We used the 158R grating, providing a dispersion of $4\text{ \AA}/\text{pix}$ and a spectral resolution of $\sim 10.5\text{ \AA}$. The typical useful spectral range is $\sim 4300\text{ \AA}$ to $\sim 9600\text{ \AA}$.

2.4 NTT

The NTT observations were carried out on 2004 August 10 to 14. To minimise the effects of differential atmospheric refraction, we observed the targets with the spectroscopic slit at the parallactic position angle (Filippenko 1982). We used grism #2 and a $1''.0$, $1''.5$ or $2''.0$ slit, depending on the seeing, which varied from $0''.7$ to $2''$. The dispersion was $3.5\text{ \AA}/\text{pix}$, the spectral resolution 9.5 \AA , and the spatial resolution $0''.33/\text{pix}$. The typical useful spectral range is $\sim 4300\text{ \AA}$ to $\sim 9700\text{ \AA}$.

2.5 VLT

The VLT observations were made in visitor mode on two occasions. On 2003 November 22 to 25, we used FORS2 on the Unit Telescope 4 Yepun, while on 2004 August 18 and 19, we used FORS1 on the Unit Telescope 2 Kueyen. Both instruments are similar, but FORS2 has higher sensitivity in the red. On both instruments, we used the 150I grism and $1''.0$ slit, providing a dispersion of $5.3\text{ \AA}/\text{pix}$ on FORS1 and $6.7\text{ \AA}/\text{pix}$ on FORS2. The spectral resolutions are $\sim 23\text{ \AA}$ and 20 \AA , and the spatial pixel scales are $0''.2/\text{pix}$ and $0''.25/\text{pix}$ for FORS1 and FORS2, respectively. The typical useful spectral range is $\sim 4000\text{ \AA}$ to $\sim 8600\text{ \AA}$ (FORS1) or 9600 \AA (FORS2). To acquire the faint targets into the slit, we used blind offsets from a nearby ($\lesssim 1'$) star in the K -band images. As the FORS instruments have a linear atmospheric dispersion corrector, we did not need to orient the slit at the parallactic angle. After the first exposure, we performed a quick data reduction. If the redshift could already be determined from this first spectrum, the next exposure was aborted to save observing time. For multiple exposures, we shifted the individual pointings by $10''$ along the slit to allow subtraction of the fringing in the red part of the detector.

2.6 Data reduction

The same standard data reduction strategy was used for all four spectrographs. After bias and flatfield correction, we removed the cosmic rays using the IRAF task `szap`. For those sources with multiple exposures shifted along the slit, we subtracted each exposure from the bracketing frame, and removed the residual sky variations using the IRAF task `background`. Next, we extracted the spectra using a width appropriate to contain all flux in the extended emission lines

(listed in column 9 of Table 2). We then calibrated the one-dimensional spectra in wavelength and flux. Finally, we corrected the spectra for Galactic reddening using the $E(B-V)$ values measured from the Schlegel et al. (1998) dust maps and the Cardelli et al. (1989) extinction law.

3 RESULTS

3.1 I -band imaging

Table 1 lists the results of our FORS2/VLT I -band imaging. Figure 1 shows the I -band images with Australia Telescope Compact Array 1.4 or 4.8 GHz radio contours (De Breuck et al. 2004, Klammer et al., in prep.) overlaid. We detect four of the ten sources to a limiting magnitude of $I \lesssim 25$. Five out of the six sources with $I > 25$ also remain undetected at K -band to a limit of $K > 20$. NVSS J230035–363410 is the only source with a K -band identification which remains undetected in I -band down to $I = 25$. This source is discussed further in §4.

3.2 Spectroscopy

Tables 2 and 3 give the results of our spectroscopy program. To date, we have observed 53 of the 76 sources in our parent sample, yielding 35 spectroscopic redshifts, shown in Figure 3 (except the three stars mentioned below). Table 3 lists the measured parameters of the emission lines in these spectra, derived using the procedures described by De Breuck et al. (2001). In some cases the uncertainties quoted are comparable to the values themselves; this is due to a combination of low signal-to-noise data and poorly determined continuum levels. Nevertheless, we include these measurements because they confirm the redshifts, and the lines appear real in the two-dimensional spectra.

Three sources show stellar spectra. Given the low sky density of radio stars (Helfand et al. 1999), and their extended radio structure, these are almost certainly foreground stars. The brightness of these stars completely outshines the background host galaxy, and we therefore exclude them from further analysis of our sample. This has no effect on the statistics of our sample.

There were 15 sources where we could not determine a spectroscopic redshift. They fell into two classes: (i) seven sources where we detected no line or continuum emission over the entire wavelength range (marked ‘undetected’ in column 2 of Table 2), and (ii) eight sources with continuum emission, but no discernible emission or absorption lines (marked ‘continuum’ in column 2 of Table 2 and shown in Fig. 2). The nature of these sources is discussed in §5.1; they constitute 29% of our sample, a fraction very similar to the 35% in the USS sample of De Breuck et al. (2001).

3.3 Photometric Redshifts

We attempted to determine photometric redshifts for the targets listed as ‘continuum’ and ‘undetected’ in Table 2, using the photometric redshift code *Z-PEG* (Le Borgne & Rocca-Volmerange 2002). In the cases where continuum was detected, we tried to fit a continuum to the

Table 3. Emission line measurements

Source	z	Line	λ_{obs} Å	Flux $10^{-16} \text{ erg s}^{-1} \text{ cm}^{-2}$	Δv_{FWHM} km s^{-1}	$W_{\lambda}^{\text{rest}}$ Å
NVSS J002219–360728	0.364±0.001	[O II] $\lambda 3727$	5083±3	10.2±2.0	550±400	25±6
		[O III] $\lambda 5007$	6833±3	5.7±1.0	700±300	15±3
NVSS J002402–325253	2.043±0.002	H α	8970±7	17.6±2.3	1600±500	100±20
		Ly α	3700±1	4.4±0.4	1150±620	130±20
		N V $\lambda 1240$	3778±1	0.15±0.03	<600	5±1
		Si IV/O IV $\lambda 1402$	4274±24	0.12±0.06	<2100	<4
		C IV $\lambda 1549$	4714±2	1.03±0.11	940±500	51±7
		He II $\lambda 1640$	4992±1	1.05±0.11	<500	53±7
		O III] $\lambda 1663$	5073±5	0.10±0.03	<7100	6±2
		C III] $\lambda 1909$	5807±1	0.87±0.09	<410	54±7
		C II] $\lambda 2326$	7074±14	0.48±0.08	2500±1100	39±8
		[Ne IV] $\lambda 2424$	7375±2	0.37±0.05	<340	31±7
		Mg II $\lambda 2800$	8516±3	0.31±0.06	<320	23±7
		[O II] $\lambda 3727$	5036±2	0.08±0.03	<460	<13
NVSS J011606–331241	0.352±0.001	[O III] $\lambda 5007$	6769±3	0.47±0.07	<430	100±25
		H α	8881±5	0.72±0.12	730±460	120±40
NVSS J015232–333952	0.618±0.001	[O II] $\lambda 3727$	6030±2	18.4±2.2	700±225	50±10
		[O III] $\lambda 4959$	8023±2	8.8±1.2	280±180	40±10
		[O III] $\lambda 5007$	8101±1	27.6±2.9	800±160	130±20
NVSS J015544–330633	1.048±0.002	Mg II $\lambda 2800$	5739±16	20.1±2.1	10400±1900	65±7
		[Ne V] $\lambda 3426$	7016±6	1.3±0.2	1300±600	6±1
NVSS J021308–322338	3.976±0.001	Ly α	6051±2	0.16±0.02	<400	40±15
NVSS J021716–325121	1.384±0.002	[O II] $\lambda 3727$	8883±1	1.29±0.15	600±130	150±50
NVSS J030639–330432	1.201±0.001	[O II] $\lambda 3727$	8203±2	11.2±1.3	800±200	21±3
NVSS J202026–372823	1.431±0.001	C III] $\lambda 1909$	4637±1	0.34±0.06	<230	11±2
		[O II] $\lambda 3727$	9060±1	3.30±0.34	700±120	110±20
NVSS J202945–344812	1.497±0.002	C III] $\lambda 1909$	4762±3	18.2±1.9	4100±540	23±2
		[Ne IV] $\lambda 2424$	6060±7	1.0±0.2	1350±650	2±0
		Mg II $\lambda 2800$	6996±6	14.1±1.5	3900±600	26±3
NVSS J213510–333703	2.518±0.001	Ly α	4278±2	1.23±0.13	1350±600	>518
NVSS J225719–343954	0.726±0.001	[O II] $\lambda 3727$	6432±1	2.91±0.30	710±160	92±12
		[O III] $\lambda 4959$	8553±2	0.99±0.15	520±220	12±2
		[O III] $\lambda 5007$	8640±1	2.75±0.30	650±140	33±4
NVSS J230123–364656	3.220±0.002	Ly α	5131±2	0.41±0.05	1200±500	80±20
NVSS J230203–340932	1.159±0.001	[O II] $\lambda 3727$	8047±2	0.54±0.06	920±250	33±5
NVSS J231144–362215	2.531±0.002	Ly α	4294±2	0.97±0.12	1600±400	...
NVSS J231338–362708	1.838±0.002	Ly α	3462±11	2.14±0.46	3100±1900	35±10
		C III] $\lambda 1909$	5417±4	0.10±0.02	<500	3±1
		C II] $\lambda 2326$	6596±5	0.15±0.07	<700	7±3
NVSS J231357–372413	1.393±0.001	[O II] $\lambda 3727$	8920±2	2.15±0.24	910±180	26±3
NVSS J231402–372925	3.450±0.005	Ly α	5411±6	0.17±0.02	1850±750	40±10
NVSS J231727–352606	3.874±0.002	O VI $\lambda 1035$	5033±15	0.17±0.19	3100±2000	22±10
		Ly α	5930±7	0.43±0.05	3000±800	75±20
		C IV $\lambda 1549$	7551±3	0.61±0.07	1250±250	45±10
NVSS J232001–363246	1.483±0.002	He II $\lambda 1640$	7991±21	0.33±0.07	2400±1200	32±10
		C IV $\lambda 1549$	3857±20	0.43±0.17	3200±2600	20±10
		He II $\lambda 1640$	4076±1	0.29±0.06	250±200	25±10
		C III] $\lambda 1909$	4733±2	0.25±0.05	500±300	20±4
		C II] $\lambda 2326$	5765±2	0.15±0.04	300±250	12±3
		[Ne IV] $\lambda 2424$	6019±11	0.05±0.04	650±350	...
		[Ne V] $\lambda 3426$	8503±26	0.48±0.15	2100±1200	25±9
		[O II] $\lambda 3727$	9253±2	2.72±0.31	750±150	150±44
		Ly α	5258±4	0.54±0.07	2300±400	65±15
		C IV $\lambda 1549$	6683±5	0.05±0.03	325±300	...
NVSS J232651–370909	2.357±0.003	He II $\lambda 1640$	7101±21	0.10±0.06	1400±900	...
		Ly α	4078±2	3.4±0.4	1000±600	280±120
		C IV $\lambda 1549$	5203±1	0.23±0.02	<440	18±2
NVSS J234145–350624	0.644±0.001	C III] $\lambda 1909$	6395±7	0.11±0.04	<750	11±5
		[O II] $\lambda 3727$	6126±3	13.5±2.1	740±260	60±15
NVSS J234904–362451	1.520±0.003	[O III] $\lambda 5007$	8238±3	10.4±1.5	800±225	80±20
		C III] $\lambda 1909$	4800±4	10.9±1.1	5500±600	26±3
		C II] $\lambda 2326$	5871±13	1.5±0.2	3500±1600	4±1
		Mg II $\lambda 2800$	7049±9	16.8±1.7	7450±900	55±6
		[O III] $\lambda 5007$	7890±22	1.0±0.2	2600±2300	4±1
		[Ne V] $\lambda 3426$	8639±3	0.9±0.1	800±300	4±1

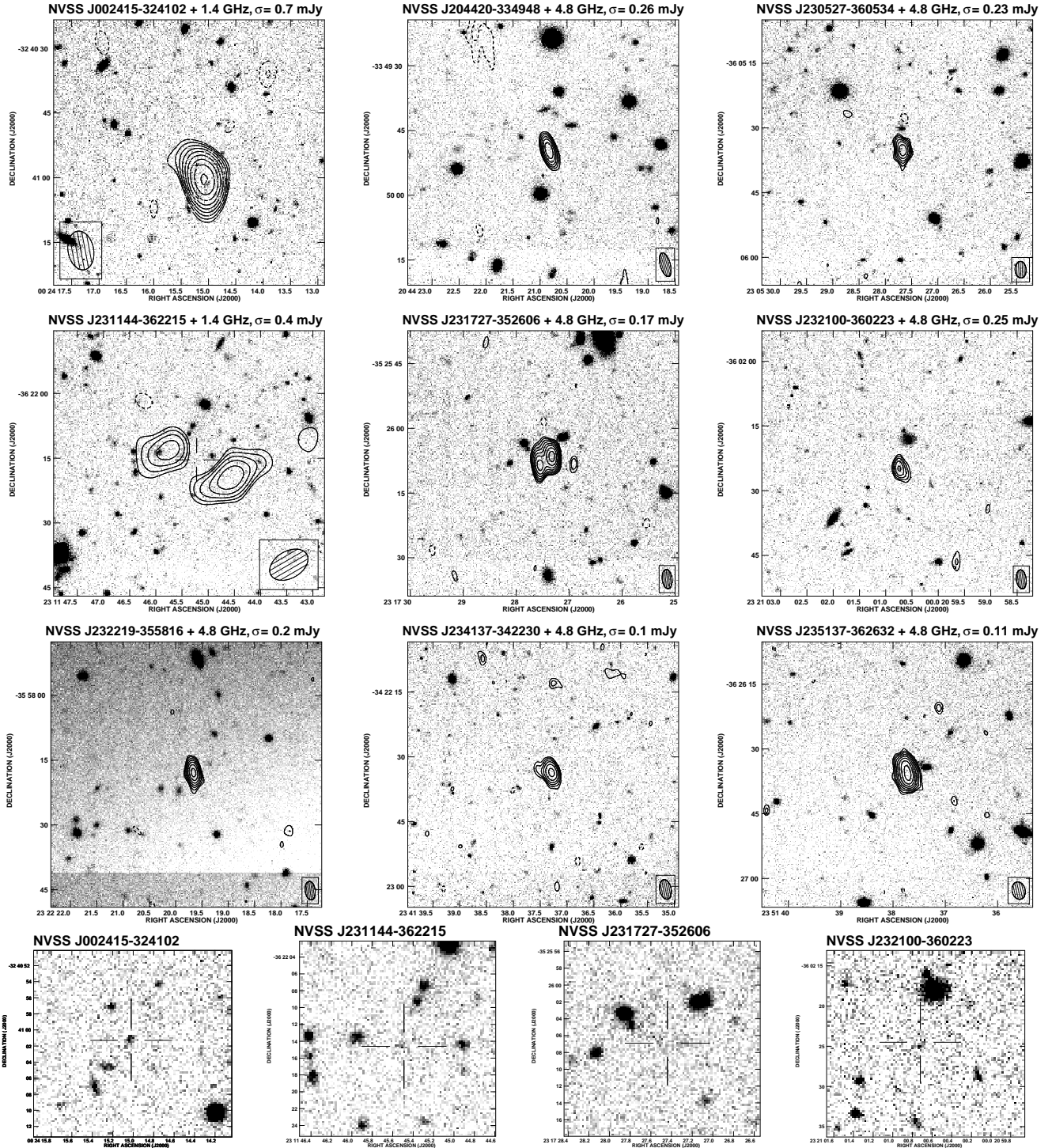


Figure 1. VLT/FORS2 *I*-band images with ATCA 1.4 or 4.8 GHz contours overlaid. The contour scheme is a geometric progression in $\sqrt{2}$. The first contour level is at 3σ , where σ is the rms noise measured around the sources, as indicated above each plot. The synthesised beam is shown in the bottom right corner. The *I*-band image of NVSS J230035–363410 is shown in Fig. 4. The bottom row shows blow-ups of the four detections.

observed *K*-band magnitude, and optical magnitudes derived from the calibrated spectra. However, the ‘undetected’ sources had no continuum, and therefore an upper limit to the optical bands was calculated from the spectra and fit along with the *K*-band magnitude in an attempt to set a

minimum redshift at which the optical emission would be below the noise limit.

We performed the same analysis for sources which had redshifts measured from the spectra. The results showed significant discrepancies between the fitted values from *Z-PEG*, and the redshifts measured from spectral features. In

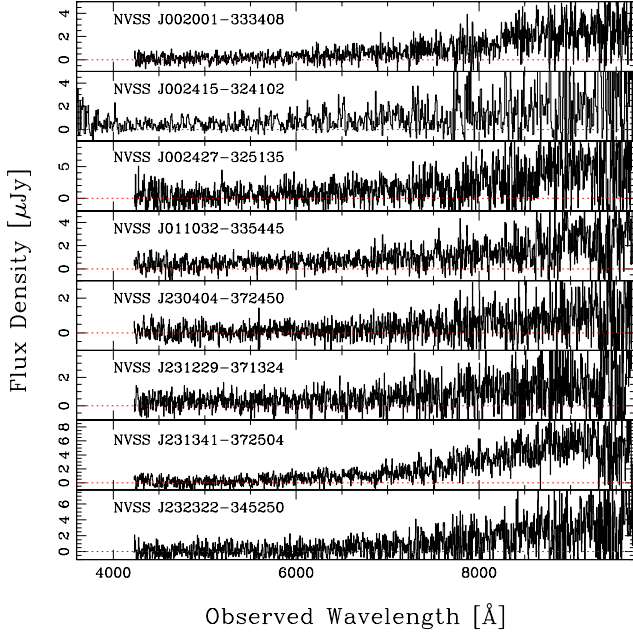


Figure 2. Spectra obtained with NTT/EMMI or VLT/FORS2 (NVSS J002415–324102 only) showing continuum emission but no identifiable features.

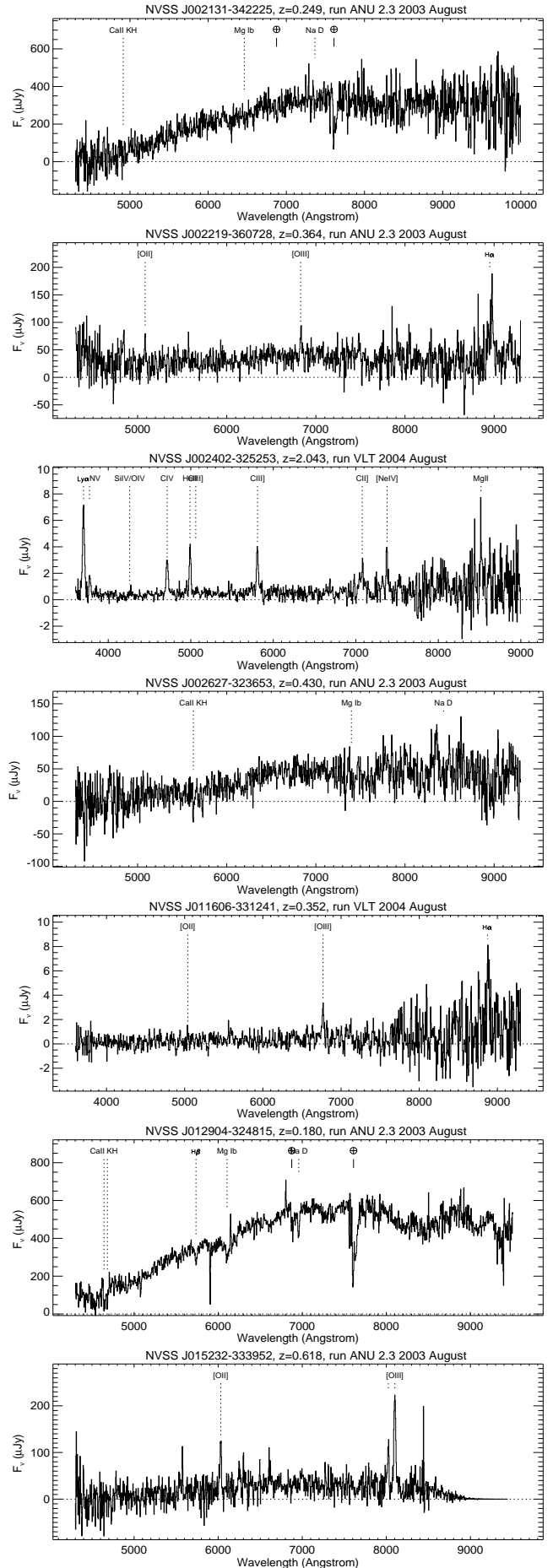
some cases, no acceptable fit to the observed colours could be found, despite a secure redshift having been determined from the spectrum. In other cases, the *Z-PEG* fits were very poorly constrained. Furthermore, there was a tendency for the fits to congregate around $z \sim 2$.

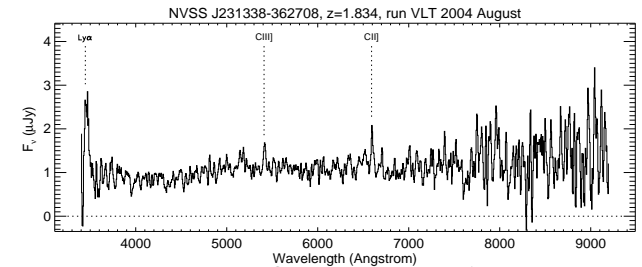
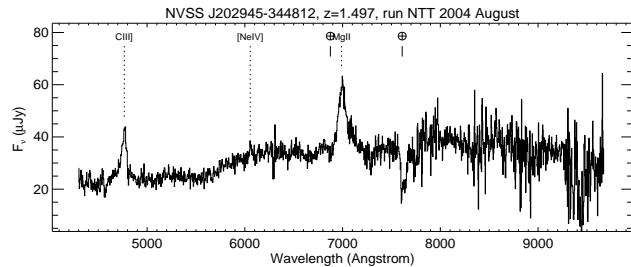
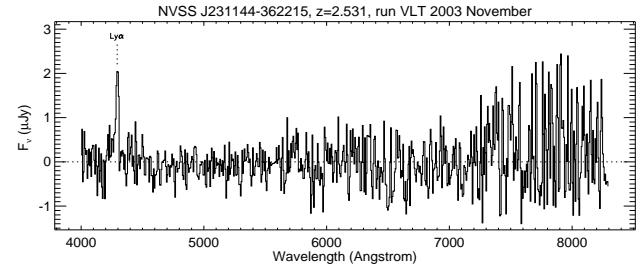
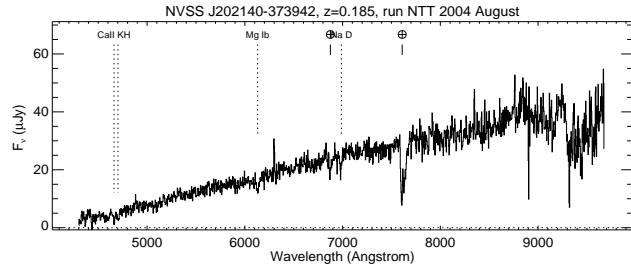
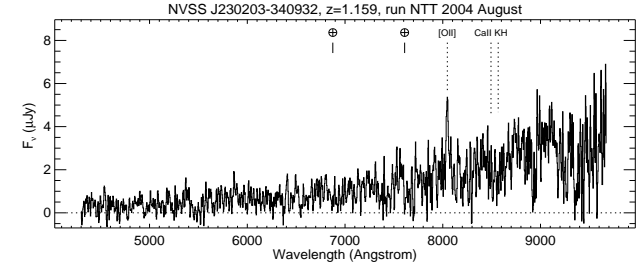
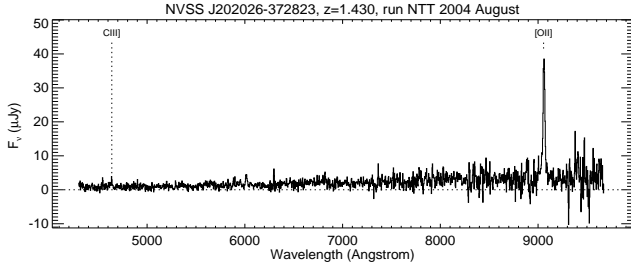
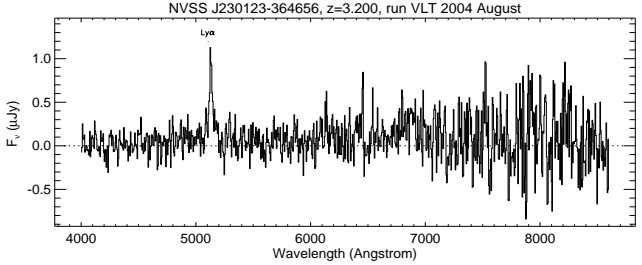
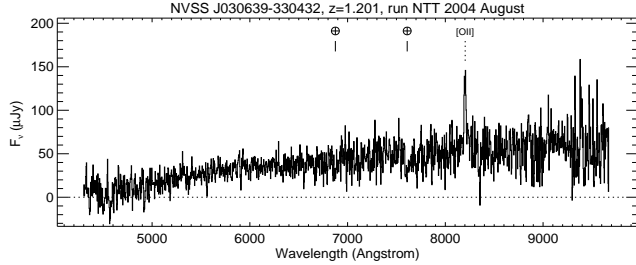
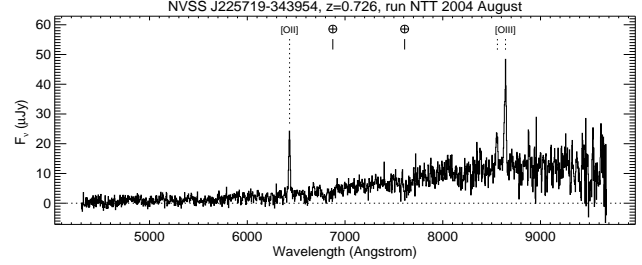
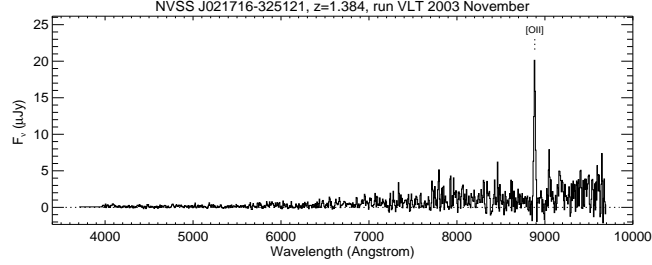
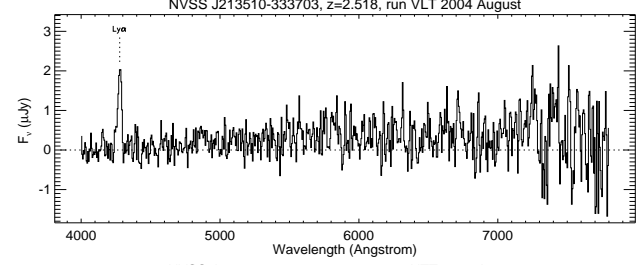
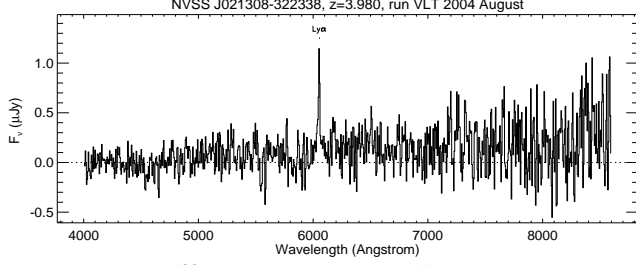
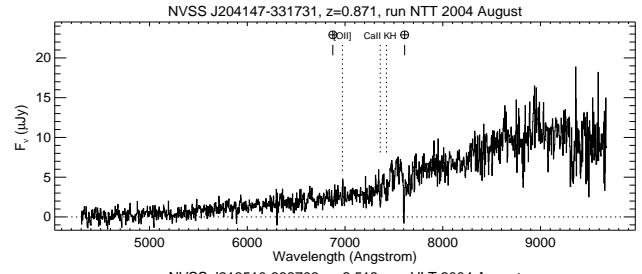
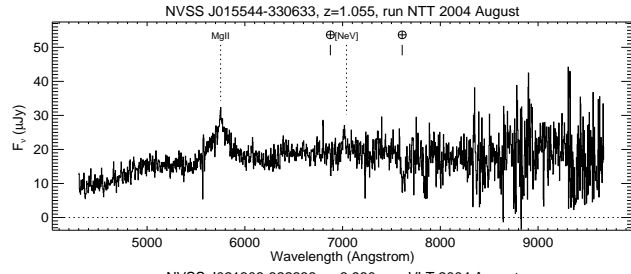
We believe that photometric redshifts could not be found for several reasons: template mismatch, absence of IR photometry, and/or dust. First, the active galaxies in our sample may have a significant contribution from direct or scattered AGN light, especially in the optical bands. If the objects are at $z > 1$, as expected from their faint *K*-band magnitudes (see §5.2.3), the optical bands trace the rest-frame UV emission, and may also be boosted by young star formation associated with the radio jet activity. In both cases our galaxies will not be well matched to the template galaxies in *Z-PEG*. Second, at the likely redshift range of our sources, $1 < z < 4$, the Balmer and 4000 Å discontinuities shift to the wavelength range ~ 0.9 to $2.0 \mu\text{m}$, a range not covered by our spectra. Willott et al. (2001b) found plausible photometric redshifts in the range $1 < z < 2$ for seven sources from the 7C Redshift Survey using *RIJHK* photometry, illustrating the importance of near-infrared photometry for these objects. Third, it is difficult to assess the amount of dust in these galaxies. The photometric redshifts were therefore not included in this paper.

3.4 Notes on individual sources

NVSS J002001–333408: The continuum is well detected (Fig. 2), but we see no emission or absorptions lines. The rise in the continuum around $\sim 8200 \text{ Å}$ is probably due to the 4000 Å break at $z \sim 1$.

NVSS J002427–325135: The continuum is well detected (Fig. 2), but we see no emission or absorption lines. The rise





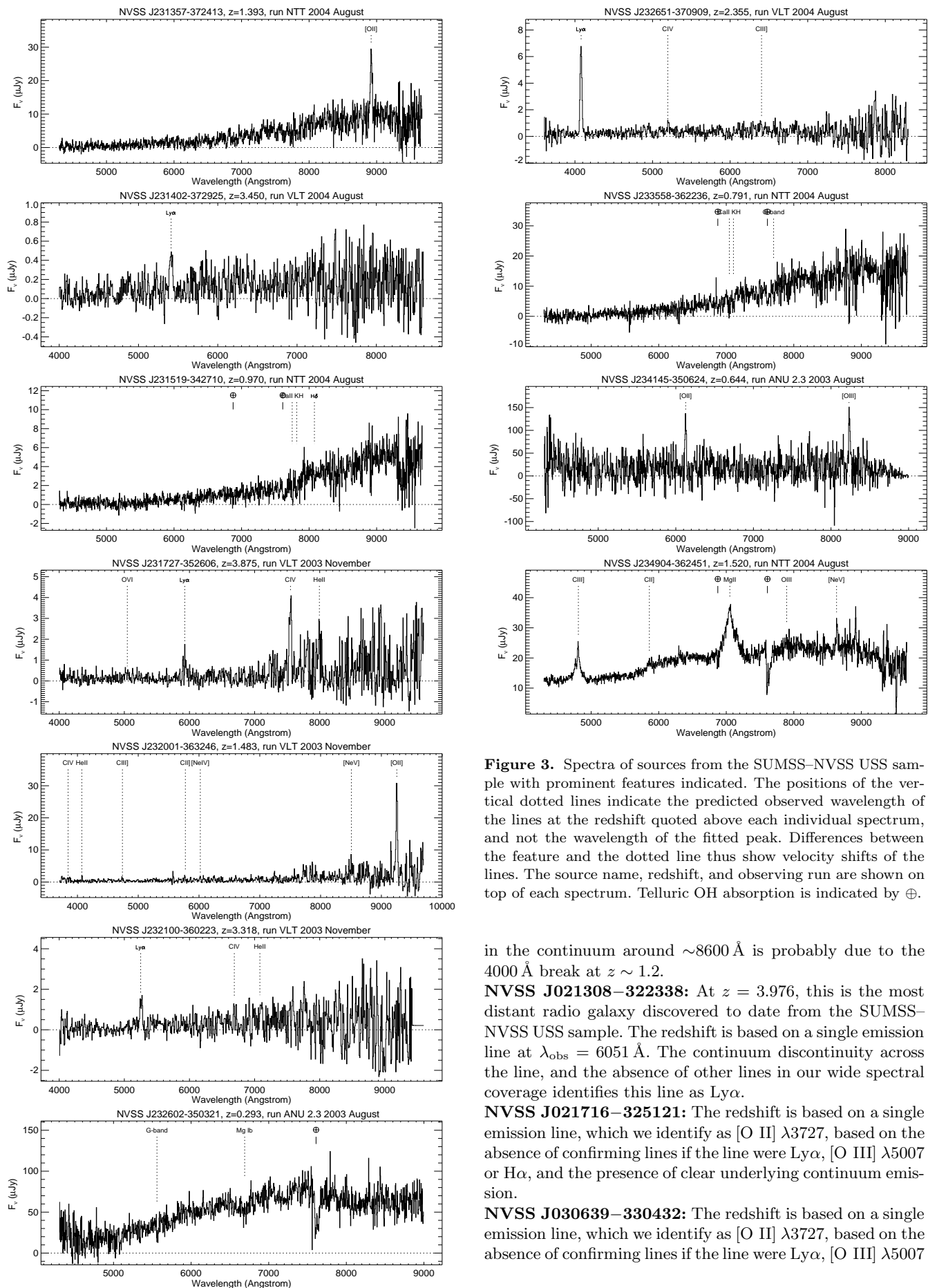


Figure 3. Spectra of sources from the SUMSS–NVSS USS sample with prominent features indicated. The positions of the vertical dotted lines indicate the predicted observed wavelength of the lines at the redshift quoted above each individual spectrum, and not the wavelength of the fitted peak. Differences between the feature and the dotted line thus show velocity shifts of the lines. The source name, redshift, and observing run are shown on top of each spectrum. Telluric OH absorption is indicated by \oplus .

in the continuum around $\sim 8600 \text{ \AA}$ is probably due to the 4000 \AA break at $z \sim 1.2$.

NVSS J021308–322338: At $z = 3.976$, this is the most distant radio galaxy discovered to date from the SUMSS–NVSS USS sample. The redshift is based on a single emission line at $\lambda_{\text{obs}} = 6051 \text{ \AA}$. The continuum discontinuity across the line, and the absence of other lines in our wide spectral coverage identifies this line as Ly α .

NVSS J021716–325121: The redshift is based on a single emission line, which we identify as [O II] $\lambda 3727$, based on the absence of confirming lines if the line were Ly α , [O III] $\lambda 5007$ or H α , and the presence of clear underlying continuum emission.

NVSS J030639–330432: The redshift is based on a single emission line, which we identify as [O II] $\lambda 3727$, based on the absence of confirming lines if the line were Ly α , [O III] $\lambda 5007$

or $H\alpha$, and the presence of clear underlying continuum emission.

NVSS J202518–355834: We observed this source at two different position angles to ensure we covered all possible identifications. However, the central object coincident with the radio source remains undetected in our VLT spectra.

NVSS J204420–334948: No line or continuum emission was detected in the 3600s FORS2 spectrum. Because of its extremely steep radio spectrum ($\alpha_{843}^{1400} = -1.60$) and favourable RA at the time of the FORS1 observations, we obtained a further 8100s spectrum. The source remains undetected, indicating either that redshift determinations of such very faint sources are beyond the capabilities of present-day optical spectrographs, or that this source may be at $z \gtrsim 7$.

NVSS J213510–333703: The redshift is based on a single emission line, which we interpret as $Ly\alpha$, based on the absence of confirming lines if the line were [O II] $\lambda 3727$, [O III] $\lambda 5007$ or $H\alpha$, and the faint continuum discontinuity across the line.

NVSS J230123–364656: The redshift is based on a single emission line, which we interpret as $Ly\alpha$, based on the absence of confirming lines if the line were [O II] $\lambda 3727$, [O III] $\lambda 5007$ or $H\alpha$, and the faint continuum discontinuity across the line.

NVSS J231144–362215: The redshift is based on a single emission line, which we interpret as $Ly\alpha$, based on the absence of confirming lines if the line were [O II] $\lambda 3727$, [O III] $\lambda 5007$ or $H\alpha$, and absence of continuum emission.

NVSS J231338–362708: This is a typical example of a source in the ‘redshift desert’, with $Ly\alpha$ detected at the very edge of the spectral coverage. The $Ly\alpha$ line is diffuse and extended, and the continuum emission is very strong. The redshift is confirmed by carbon lines.

NVSS J231341–372504: The continuum is well detected (Fig. 2), but we see no emission or absorption lines. The rise in the continuum around $\sim 7500 \text{ \AA}$ is probably due to the 4000 \AA break at $z \sim 0.9$.

NVSS J231357–372413: The redshift is based on a single emission line, which we identify as [O II] $\lambda 3727$, based on the absence of confirming lines if the line were $Ly\alpha$, [O III] $\lambda 5007$ or $H\alpha$, and the presence of clear underlying continuum emission.

NVSS J231402–372925 The redshift is based on a single emission line, which we interpret as $Ly\alpha$, based on the absence of confirming lines if the line were [O II] $\lambda 3727$, [O III] $\lambda 5007$ or $H\alpha$, and the continuum discontinuity across the line.

NVSS J232001–363246: This source is at lower redshift than expected from the $K-z$ relation (see also §5.2.3). Both the redshift and identification of the radio source are secure.

NVSS J232219–355816: Because no optical counterpart was detected down to $I \sim 25$, we did not attempt to obtain a spectrum.

NVSS J235137–362632: Because no optical counterpart was detected down to $I \sim 25$, we did not attempt to obtain a spectrum.

4 EFFICIENCY OF THE HOST GALAXY IDENTIFICATION PROCEDURE

In paper I, we have used $5\text{--}10''$ resolution radio images to identify the host galaxies of the USS sources in deep K -band images (reaching $K = 21$ for the faintest sources). Previous USS searches have mostly used $\sim 1''$ resolution radio maps (e.g. Lacy et al. 1992; Röttgering et al. 1994; Chambers et al. 1996; Blundell et al. 1998; De Breuck et al. 2000), and optical (R - or I -band) or K -band imaging. Here we discuss the efficiency of our identification procedure based on the data obtained to date.

It is possible that our relatively low resolution radio maps may have led to a higher fraction of mis-identifications. We can, however, use some prior information to determine if the spectroscopically observed object is the correct host galaxy of the USS radio source. One important tool is the Hubble $K-z$ diagram (see also §5.2.3). De Breuck et al. (2002) show that the hosts of radio galaxies are likely to be about 2 magnitudes brighter than normal star-forming galaxies at the same redshift. Coupled to the rarity of radio galaxies (e.g. Willott et al. 2001a) compared with normal star-forming galaxies (e.g. Seymour et al. 2004), this means that a mis-identification would most likely be made with a normal galaxy (as opposed to another radio galaxy host), several magnitudes fainter than expected for its redshift. In other words, the faintest near-IR ($K \geq 19.5$) galaxies in our sample are expected to be associated with the hosts of radio galaxies at redshifts beyond $z \sim 1$. A mis-identification of these hosts would most likely lead to galaxies in the redshift range $0.3 \lesssim z \lesssim 1$. Nine of the ten galaxies we observed with $K \geq 19.5$ have resulted in spectroscopically confirmed redshifts beyond 1.3, from which we conclude that their identifications are reliable. The tenth turned out to be at $z = 0.826 \pm 0.002$ and we consider this to be unreliable (see below).

Of the 37 USS radio sources for which we present spectroscopic redshifts in this paper, four are clearly misidentified with foreground objects, with a fifth identification which we regard with skepticism. As mentioned in §3.2, three host galaxy candidates (NVSS J231016–363624, NVSS J202856–353709 and NVSS J231016–363624) turned out to be foreground stars. The fourth misidentification was the target associated with NVSS J230035–363410. In this case, its 20cm radio morphology (Figure 4, *top*) is extended, making a clear identification difficult. Optical imaging revealed an $I = 24.6$ galaxy located at **b** on Figure 4 (*top*) to be the most likely candidate. Follow-up spectroscopy determined the redshift of this galaxy to be $z = 0.826 \pm 0.002$, based on [O II] $\lambda 3727$ and [O III] $\lambda 5007$ lines at $\lambda_{\text{obs}} = 6806 \text{ \AA}$ and 9146 \AA , respectively. According to the best-fitting $K-z$ relation for 3C, 6C and 7C radio galaxies (Willott et al. 2003), the expected K -band magnitude for a $z = 0.826 \pm 0.002$ radio galaxy with a radio luminosity typical of a 7C source is 17.26 ± 0.1 . We became skeptical about the reliability of the identification of NVSS J230035–363410 based on its faint infra-red magnitude ($K > 20$), a $> 27\sigma$ deviation from the $K-z$ relation. We have since obtained higher spatial resolution ($3''.9 \times 2''.6$) radio observations at 4.8 GHz and 6.2 GHz (Fig. 4, *bottom*; Klammer et al, in prep), which indicate that the position of the radio core is located several arcseconds south-east of **b**,

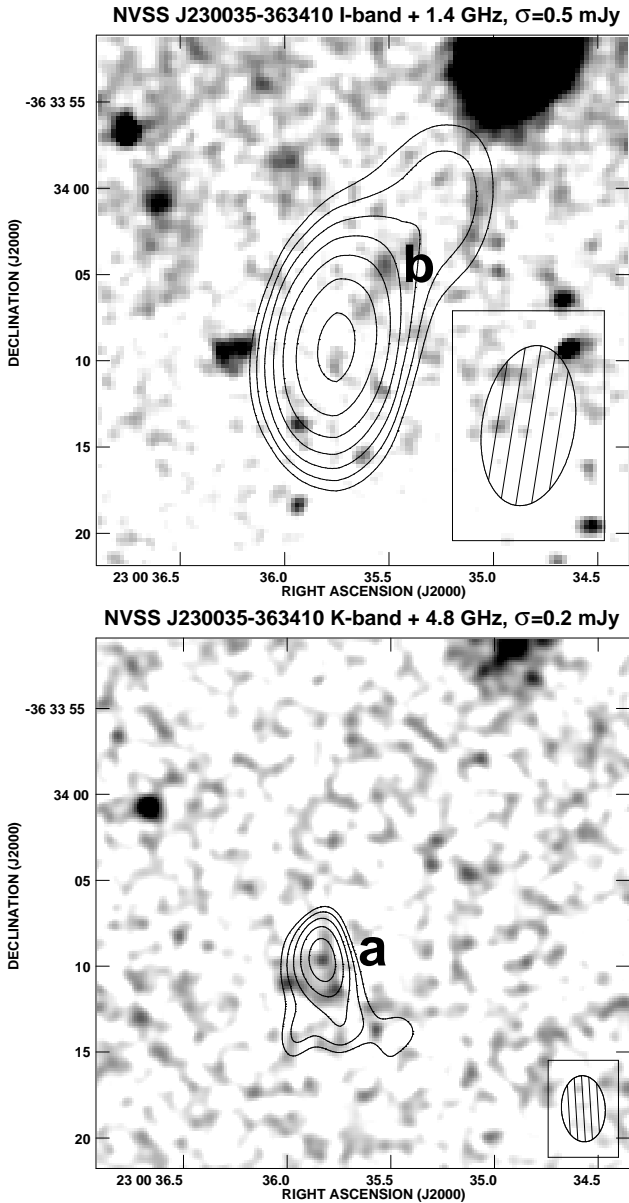


Figure 4. *Top:* ATCA 1.4 GHz image of NVSS J230035–363410 from paper I overlaid on a VLT/FORS2 *I*–band image. *b* marks the initial identification. Object *a* is not detected to a limiting magnitude of $I=25$. *Bottom:* ATCA 4.8 GHz image overlaid on the NTT/SofI *K*–band image from paper I. This radio image clearly identifies object *a* as the host galaxy, illustrating the importance of high-resolution radio maps and *K*–band, rather than *I*–band imaging. Object *b* is not detected to a limiting magnitude of $K=20.6$. The contour scheme is a geometric progression in $\sqrt{2}$. The first contour level is at 3σ , where σ is the rms noise measured around the sources, as indicated above each plot. The synthesised beams are indicated in the lower right corners.

coincident with a $K = 19.8$, $I > 25$ galaxy labeled **a** on Figure 4 (*bottom*). In this case, deep *I*–band imaging was counter-productive to our identification process, but we were able to recognise the error by comparing its predicted versus measured location on the $K - z$ diagram.

In a similar context, the $z = 0.352$ galaxy identified with NVSS J011606–331241 is much fainter than expected,

deviating by 13σ from the $K - z$ relation for 7C radio galaxies (Willott et al. 2003). Therefore, it is possible we have also misidentified this host galaxy with a foreground object, although there are examples of similar $K - z$ outliers with secure host galaxy identifications (Willott et al. 2003). A close inspection of the *K*–band image reveals a much fainter object approximately $0''.5$ to the West. Higher spatial resolution radio observations are necessary in order to increase the sensitivity and positional accuracy of the radio emission in order to determine if this fainter source could be the true host galaxy. Alternatively, the $z = 0.352$ galaxy may be a foreground galaxy acting as a gravitational lens of an as yet undetected background radio galaxy. Our NTT *K*–band image (see Fig. 2 in paper I) does not show any clear signs of lensing; deeper optical and/or near-IR images with high spatial resolution would be needed to test this hypothesis.

5 DISCUSSION

With spectroscopic observations for 50 out of 73 sources¹ (39 out of 51 if we consider only the sources with $\alpha_{843}^{1400} < -1.3$) in our sample, we can now start looking at the statistical properties of our sample. Although we have been able to determine only 35 spectroscopic redshifts, our deep spectra do provide constraints on the redshifts of the other 15 sources (§5.1). Most of our spectra are of insufficient quality to derive much physical information about the host galaxies or their extended emission-line regions. However, with the redshift information, we are now in a position to interpret their *K*–band fluxes in terms of stellar populations, and compare them with other samples of radio galaxies (§5.2). Finally, the redshift information for $43/73 = 59\%$ of the sample, including five sources at $z > 3$, allows us to put strong lower limits on the space densities of these massive galaxies at high redshift (§5.4).

5.1 The nature of the continuum-only and undetected objects

We first discuss the nature of the sources where we detected only continuum emission (Fig. 2), or which remained undetected in medium-deep VLT exposures. The continuum sources have mainly been observed with the NTT. It is likely that deeper observations with 8–10m class telescopes may yield a spectroscopic redshift. The detection of continuum emission down to $\sim 4000 \text{ \AA}$ indicates that the Ly α discontinuity in these sources must be bluewards of this, and hence we can constrain their redshifts to $z \lesssim 2.3$. On the other hand, if the [O II] $\lambda 3727$ line was at wavelengths free of strong night sky lines ($\lambda_{\text{obs}} < 7200 \text{ \AA}$), we would probably have detected it, so the likely redshift range is $1 < z < 2.3$, corresponding to the ‘redshift desert’. These 8 sources are thus likely to be high redshift radio galaxies with relatively faint emission lines, either intrinsically or due to dust obscuration.

Of the six undetected sources, one was observed with

¹ We have excluded the three objects obscured by foreground stars.

the NTT, and may be detected with more sensitive observations. The remaining five sources are extremely faint, and are beyond the capabilities of present-day optical spectrographs. The WN/TN USS sample of De Breuck et al. (2001) contains seven such undetected USS sources in ~ 1 hour Keck spectra; all have unresolved radio morphologies $\lesssim 1''.5$. Of the five undetected sources in the SUMSS–NVSS USS sample, four have unresolved radio structures with sizes $< 6''$, and only NVSS J015223–333833 is resolved: a $15''$ radio double. They also have some of the steepest radio spectral indices in our USS sample with $\alpha_{843}^{1400} < -1.55$ (where $S_\nu \propto \nu^\alpha$). This, combined with their faint K -band identifications (two sources have $K > 20.5$) suggests these sources may be at $z \gtrsim 7$, where Ly α has shifted out of the optical passband. We have started a near-IR spectroscopy campaign on these sources with the Gemini-South telescope to search for emission lines shifted into the J band.

An alternative explanation is that the undetected sources are heavily obscured by dust. This is likely to be the case in a significant fraction of the undetected WN/TN USS sources (De Breuck et al. 2001), since at least half show strong (sub)mm thermal dust emission (Reuland et al. 2003; Reuland 2005). Sub-mm observations of these sources with the Large Apex Bolometer Camera (LABOCA) on the Atacama Pathfinder Experiment (APEX) should allow us to determine if they are indeed strong dust emitters. Optical and near-IR redshift determination may then prove unfeasible, and alternatives such as observing the rotational transitions of CO may be needed. Targeted searches will become possible in the near future with the wide-bandwidth correlator on the Australia Telescope Compact Array, and later with the wide bandwidth receivers of the Atacama Large Millimetre Array (ALMA).

5.2 The K - z relation

Figure 5 shows the K -band magnitudes versus redshifts for the sources in Table 2, along with corresponding data from several radio catalogues listed in the caption. We converted the $8''$ -diameter aperture magnitudes from paper I to 64 kpc metric apertures using the procedures described by Eales et al. (1997). This consists of using the Sandage (1972) curve of growth for radio galaxies at $z < 0.6$ and a radial profile $\propto r^{0.35}$ for radio galaxies at $z > 0.6$.

5.2.1 Contribution from emission lines

The small scatter in the $K - z$ relation is attributed to the stellar contribution to the K -band magnitude. However, at some redshifts strong emission lines can boost the K -band magnitude, offsetting the distribution towards brighter K -band magnitudes. Our optical spectroscopy has shown that most of the galaxies have apparently strong emission lines (see Table 3). However, our SUMSS–NVSS sample contains sources with radio luminosities which are almost an order of magnitude lower than those in flux-limited radio surveys such as 3C, 6C and 7C. The strong correlation between radio and emission line luminosity (Willott et al. 1999) thus predicts much weaker emission lines, which will also contribute less to the broad-band fluxes (see also Jarvis et al. 2001; Rocca-Volmerange & Remazeilles 2005).

The most important emission-line contribution to the K -band flux would come from H α , [O II] $\lambda 3727$ and [O III] $\lambda 5007$ (De Breuck et al. 2002) at redshifts around $z \sim 2.3$, 3.4 and 4.9. While two of the three measured points on our $K - z$ plot around $z \sim 3.4$, have slightly brighter K -band magnitudes than the fitted line, they are still within the expected scatter and are therefore not obviously affected by emission-line contributions. Conversely, at $z \sim 2.3$ the scatter is towards fainter K -band magnitudes. Therefore, there is no strong evidence in our $K - z$ distribution for contamination of the K -band magnitudes by emission lines.

5.2.2 Dispersion in the $K - z$ relation

The dispersion in the K -band magnitudes along the $K - z$ diagram has been used as an indicator of the evolution of the stellar population in powerful galaxies (Eales et al. 1997; Jarvis et al. 2001; Willott et al. 2003; Rocca-Volmerange et al. 2004). We calculated the dispersion of the measured K -band magnitudes from the line of best fit (Paper I) and compared this value in redshift bins. Galaxies in each unit of redshift from $z = 0-1$ up to $z = 3-4$ had standard deviations of 1.1, 1.0, 0.7 and 0.8 respectively. The standard deviation for $z < 2$ was 1.0, decreasing to 0.7 for $z > 2$.

Eales et al. (1997) found an increase in the dispersion of K -band magnitude for $z > 2$ galaxies and used this to support their model that $z > 2$ is the epoch of galaxy formation. Our results do not support this model, but instead we see a slight decrease in dispersion at higher redshifts, which is more consistent with the observations of Jarvis et al. (2001). We need to caution that if there is a significant contribution to the K -band magnitude from non-stellar emission (scattered or transmitted AGN light, emission lines), then the assumption that the dispersion in the $K - z$ plot is indicative of the stellar evolution is compromised.

While redshifts have not been measured for our complete sample, the low scatter around the $K - z$ relation seems at least consistent with a model in which the epoch of formation of ellipticals may be at a similar high redshift ($z > 4$), with passive evolution since then. At $z > 1$, the SUMSS–NVSS sources also appear slightly fainter than the 3C, 6C and 7C radio galaxies. If the K -band light is indeed dominated by stars, this can be interpreted as a lower average mass in the range 10^{11} – $10^{12} M_\odot$ (Rocca-Volmerange et al. 2004). This would be consistent with the lower radio luminosities of the SUMSS–NVSS sources implying less massive central black holes in their host galaxies.

5.2.3 Accuracy of the $K - z$ relation as a redshift indicator

In Paper I we used the $K - z$ relation to predict the median redshift of our sample to be 1.75. The distribution of measured redshifts for our sample is shown in Fig. 5, with a median z of 1.2. If the galaxies listed as ‘undetected’ in Table 2 are not detected because they are at high redshift (at least $z > 1.75$), then this would shift the median z up to 1.5. There also remains a further 23 sources for which the redshift is yet to be determined; 15 of the 23 are faint enough

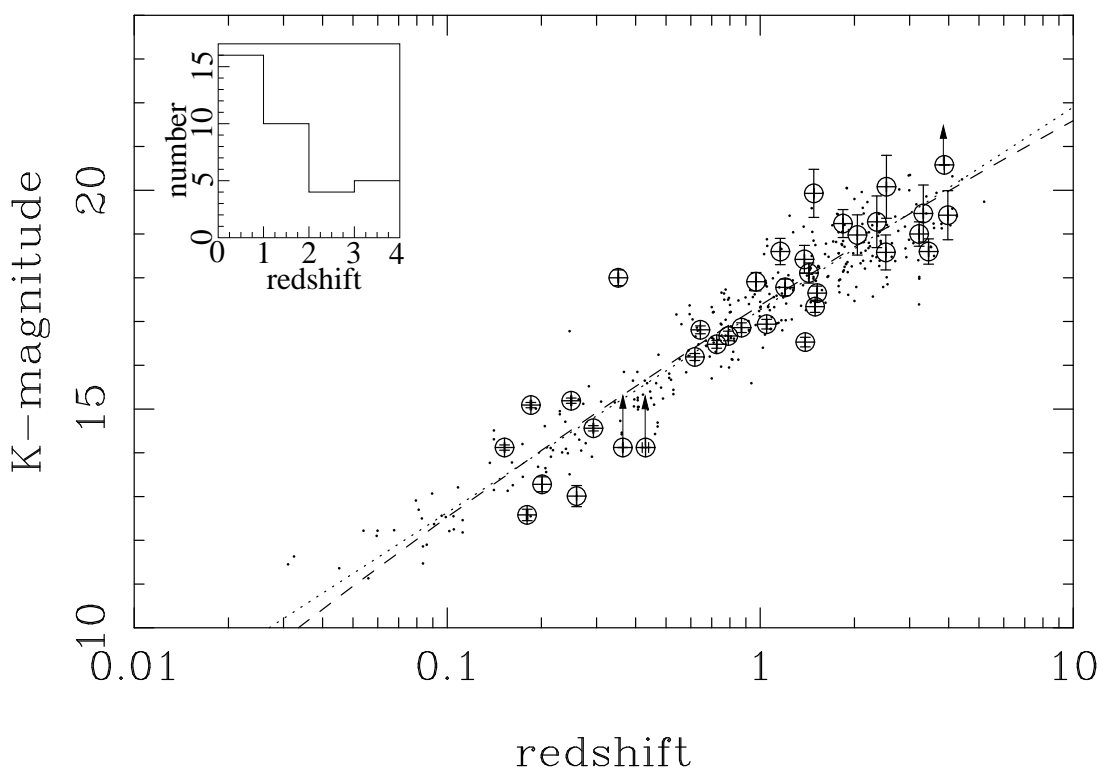


Figure 5. K -band magnitude corrected to a 64 kpc metric aperture versus redshift. The sources with measured redshifts in Table 2 are shown by the large circles. In some cases the K -band magnitude uncertainties are smaller than the circles, and the redshift uncertainties are all much smaller than the circles. The dots comprise a number of radio catalogues; the 3CRR, 6CE, 6C and 7CRS radio galaxy samples (compiled by Willott et al. 2003) and the composite samples of van Breugel et al. (1998) and De Breuck et al. (2002). The dotted line is the fit to the galaxy samples (dots) from Paper I, while the dashed line is the fit to the galaxy sample from Willott et al. (2003). Inset is the histogram of the redshifts for the 35 sources measured in this paper.

($K[8''] > 18.3$) to lie at $z > 1.75$, therefore increasing the median z to at least 1.75. Therefore we anticipate that the median redshift will be close to that predicted when we have spectroscopic redshifts for the complete sample.

The redshift distribution from the $K-z$ relation included at least three galaxies with $z > 4$. Follow-up spectroscopy has yet to find any galaxies with $z > 4$. The best fit to the radio galaxy $K-z$ relation predicts $z > 4$ for $K > 20.06$ host galaxies. Of the four galaxies in our sample that have $K(64 \text{ kpc}) > 20.06$, two have yet to be observed spectroscopically, and the remaining two have redshifts measured to be 2.531 and 1.483. The latter galaxy is on the extremities of the K -band magnitude distribution for radio galaxies, and while the former target is within the scatter, it is far from the predicted $z = 4$. Conversely, a target predicted from the K -magnitude, to be at $z = 2.15$ turned out to be at $z = 3.450$. This highlights one of the shortcomings of the $K-z$ plot, namely that there is a broad range of redshifts for any given K -band magnitude. Despite this, the $K-z$ relation remains a useful tool for predicting redshift when planning follow-up spectroscopy.

5.3 Surface density of SUMSS–NVSS USS radio galaxies at $z > 3$

As noted in paper I, the surface density of USS radio sources selected from NVSS and SUMSS (482 sr^{-1}) is more than four times higher than that of USS sources selected by

Table 4. Redshift distribution of USS sources from this sample and De Breuck et al. (2001). Objects with spectral index $\alpha > -1.3$ have been excluded from the statistics.

	This paper		De Breuck et al. (2001)	
$z < 3$	23	$59 \pm 12\%$	37	$61 \pm 10\%$
$z > 3$	5	$13 \pm 6\%$	11	$18 \pm 5\%$
Continuum	5	$13 \pm 6\%$	6	$10 \pm 4\%$
Undetected	6	$14 \pm 6\%$	7	$11 \pm 4\%$
Total	39		61	

De Breuck et al. (2000, 2002) from the WENSS and NVSS surveys (103 sr^{-1} to the same 1.4 GHz flux density limit of 15 mJy). We now ask whether the higher surface density of SUMSS–NVSS objects translates into a correspondingly higher surface density of high-redshift radio galaxies. Table 4 compares the redshift distribution of USS objects from the two surveys. The fraction of $z > 3$ objects in the SUMSS–NVSS sample is similar to that found by De Breuck et al. (2000, 2002), implying that USS selection at 843–1400 MHz is also an efficient way of selecting $z > 3$ radio galaxies.

We can use the results in Table 4, together with the known surface density of USS radio sources, to estimate a minimum surface density for powerful radio galaxies at $z > 3$. If $13 \pm 6\%$ of SUMSS–NVSS USS radio sources lie at $z > 3$,

then the minimum surface density of $z > 3$ radio galaxies is $63 \pm 29 \text{ sr}^{-1}$. This is higher than the corresponding value for the WENSS–NVSS USS sample ($19 \pm 5 \text{ sr}^{-1}$), implying that the SUMSS–NVSS selection method can identify about three times as many genuine $z > 3$ objects per unit area of sky as the WENSS–NVSS selection.

5.4 Space density of radio galaxies at $3 < z < 4$

For $3 < z < 4$, the 1.4 GHz flux limit of the SUMSS–NVSS sample corresponds to a minimum radio power of roughly $10^{27.0}$ to $10^{27.2} \text{ W/Hz}$. For USS radio galaxies above this luminosity, using the surface densities derived above, we can estimate a minimum space density of roughly $1.2 \pm 0.6 \times 10^{-9} \text{ Mpc}^{-3}$. This is very close to the density of powerful steep-spectrum radio galaxies predicted at $3 < z < 4$ by Dunlop & Peacock (1990), using models based on a complete sample of radio sources selected at 2.7 GHz. Their models show a gradual (but modest) decline in the space density of powerful radio galaxies over the range $z \sim 2 - 4$. Our current data are consistent with these models if USS radio galaxies represent the majority of powerful radio galaxies at $z > 3$. If there are also significant numbers of $z > 3$ radio galaxies with $\alpha > -1.3$ (which would not be detected in our current survey), then the space density of powerful radio galaxies at these redshifts would be higher than predicted by the Dunlop & Peacock models.

6 CONCLUSIONS

Based on optical spectroscopy of 53/76 of the sources in the SUMSS–NVSS USS sample, we draw the following conclusions:

- We obtain 35 spectroscopic redshifts, including five radio galaxies at $z > 3$. We also found three quasars at $1 < z < 1.6$.
- Seven sources show only continuum emission, with no clear emission or absorption lines. These are probably sources at $1 \lesssim z \lesssim 2.3$, which are either intrinsically faint or obscured by dust.
- Eight sources remain undetected in 0.5–2.25 hour deep VLT spectra. These sources could be either heavily obscured by dust, or they could be at $z \gtrsim 7$.
- We have obtained I –band imaging of 10 USS sources down to $I \approx 25$; this turned out to be counter-productive in identifying the host galaxies. Medium deep K –band imaging combined with high-resolution ($< 5''$) radio imaging is a more efficient identification procedure.
- The SUMSS–NVSS radio galaxies generally follow the $K - z$ relation defined by other radio galaxies, with one notable exception, which may be a gravitationally amplified object. The dispersion about the $K - z$ relation slightly decreases at $z > 2$, contrary to the results seen in the 6CE sample (Eales et al. 1997), and more consistent with the 6C* USS sample (Jarvis et al. 2001).
- We derive a strict lower limit on the space density of $3 < z < 4$ radio galaxies of $1.2 \pm 0.6 \times 10^{-9} \text{ Mpc}^{-3}$.

The five new $z > 3$ objects discovered from this sample bring the total number of known $z > 3$ radio galaxies in the southern hemisphere from 7 to 12, compared to 19 in the

northern hemisphere. These new sources now provide sufficient targets for detailed follow-up studies with large optical and (sub)millimetre facilities in the southern hemisphere.

7 ACKNOWLEDGEMENTS

This work was supported by PICS/CNRS (France) and IREX/ARC (Australia).

REFERENCES

- Appenzeller, I., Stahl, O., Kieseewetter-K., S., Kudritzki, R., Nicklas, H., & Rupprecht, G. 1997, in: The early universe with the VLT, ed. J. Bergeron, Springer, Heidelberg, New York, p. 35
- Baugh, C., Cole, S., & Frenk, C., Sept. 1996, *MNRAS*, 282, L27
- Baugh, C., et al. 2005, *MNRAS*, 356, 1191
- Bicknell, G., Sutherland, R., van Breugel, W., Dopita, M., Dey, A., & Miley, G. 2000, *ApJ*, 540, 678
- Blundell, K., Rawlings, S., Eales, S., Taylor, G., & Bradley, A. 1998, *MNRAS*, 295, 265
- Bock, D., Large, M., & Sadler, E.M. 1999, *AJ*, 117, 1578
- Cardelli, J., Clayton, G., & Mathis, J. 1989, *ApJ*, 345, 245
- Chambers, K., Miley, G., van Breugel, W., Bremer, M., Huang, J.-S., & Trentham, N. 1996, *ApJS*, 106, 247
- Chapman, S., Windhorst, R., Odewahn, S., Yan, H., & Conselice, C., *ApJ*, 599, 92
- Cimatti, A., et al. 2004, *Nature*, 430, 184
- Cole, S., 1991, *ApJ*, 367, 45
- Colless, M., et al. 2001, *MNRAS*, 328, 1039
- Condon, J., et al. 1998, *AJ*, 115, 1693
- Cowie, L., Songaila, A., Hu, E., & Cohen, J. 1996, *AJ*, 112, 839
- Croton, D., et al. 2005, *MNRAS*, submitted, astro-ph/0508046
- Cutri, R., et al. 2003, VizieR Online Data Catalog, 2246, 0
- Daddi, E., et al. 2000, *A&A*, 361, 535
- De Breuck, C., van Breugel, W., Röttgering, H., & Miley, G. 2000, *A&AS*, 143, 303
- De Breuck, C., et al. 2001, *AJ*, 121, 1241
- De Breuck, C., van Breugel, W., Stanford, S. A., Röttgering, H., Miley, G., & Stern, D. 2002, *AJ*, 123, 637
- De Breuck, C., et al. 2003, *A&A*, 401, 911
- De Breuck, C., Hunstead, R., Sadler, E., Rocca-Volmerange, B., & Klammer, I., 2004, *MNRAS*, 347, 837
- Devriendt, J., & Guiderdoni, B., 2000, *A&A*, 363, 851
- Dey, A., van Breugel, W., Vacca, W., & Antonucci, R. 1997, *ApJ*, 490, 698
- Dunlop, J., & Peacock, J. 1990, *MNRAS*, 247, 19
- Dunlop, J., et al. 1996, *Nature*, 381, 581
- Eales, S., Rawlings, S., Law-Green, D., Cotter, G., & Lacy, M. 1997, *MNRAS*, 291, 593
- Filippenko, A. 1982, *PASP*, 94, 715
- Fragile, P., Murray, S., Anninos, P., & van Breugel, W. 2004, *ApJ*, 604, 74
- Granato, G., De Zotti, G., Silva, L., Bressan, A., & Danese, L. 2004, *ApJ*, 600, 580
- Helfand, D., Schnee, S., Becker, R., White, R., & McMahon, R. 1999, *AJ*, 117, 1568

- Ivison, R., et al. 2002, *MNRAS*, 337, 1
- Jarvis, M., et al. 2001, *MNRAS*, 326, 1585
- Jimenez, R., Friaca, A., Dunlop, J., Terlevich, R., Peacock, J., & Nolan, L. 1999, *MNRAS*, 305, L16
- Kauffmann, G., Colberg, J. M., Diaferio, A., & White, S., 1999a, *MNRAS*, 303, 188
- Kauffmann, G., Colberg, J. M., Diaferio, A., & White, S., 1999b, *MNRAS*, 307, 529
- Kauffmann, G., White, S., & Guiderdoni, B., 1993, *MNRAS*, 264, 201
- Klamer, I., Ekers, R., Sadler, E., & Hunstead, R. 2004, *ApJ*, 612, L97
- Klamer, I., Ekers, R., Sadler, E., Weiss, A., Hunstead, R., & De Breuck, C. 2005, *ApJ*, 621, L1
- Kodama, T., et al. 2004, *MNRAS*, 350, 1005
- Lacy, M., Rawlings, S., & Warner, P. 1992, *MNRAS*, 256, 404
- Le Borgne, D. & Rocca-Volmerange, B. 2002, *A&A*, 386, 446
- Lilly, S & Longair, M. 1984, *MNRAS*, 211, 833
- Papadopoulos, P., et al. 2000, *ApJ*, 528, 626
- Rawlings, S., & Jarvis, M. 2004, *MNRAS*, 355, L9
- Rees, M. 1989, *MNRAS*, 239, 1P
- Reuland, M., van Breugel, W., Röttgering, H., de Vries, W., De Breuck, C., & Stern, D. 2003, *ApJ*, 582, 71
- Reuland, M., PhD thesis, Universiteit Leiden, 2005, available from <http://www.strw.leidenuniv.nl/events/reuland/thesis.pdf>
- Rocca-Volmerange, B., Le Borgne, D., De Breuck, C., Fioc, M., & Moy, E. 2004, *A&A*, 415, 931
- Rocca-Volmerange, B., & Remazeilles, M. 2005, *A&A*, 433, 73
- Rodgers, A., Conroy, P., & Bloxham, G. 1988, *PASP*, 100, 626
- Röttgering, H., Lacy, M., Miley, G., Chambers, K., & Saunders, R., *A&AS*, 108, 79
- Röttgering, H., Van Ojik, R., Miley, G., Chambers, K., Van Breugel, W., & de Koff, S. 1997, *A&A*, 326, 505
- Sandage, A. 1972, *ApJ*, 173, 485
- Schlegel, D., Finkbeiner, D., & Davis, M. 1998, *ApJ*, 500, 525
- Seymour, N., McHardy, I., & Gunn, K. 2004, *MNRAS*, 352, 131
- Spergel, D., et al. 2003, *ApJS*, 148, 175
- Stevens, J., et al. 2003, *Nature*, 425, 264
- Treu, T., Ellis, R., Liao, T., & van Dokkum, P. 2005, *ApJ*, 622, L5
- van Breugel, W., Stanford, S. A., Spinrad, H., Stern, D., & Graham, J. 1998, *ApJ*, 502, 614
- White, S., & Frenk, C., 1991, *ApJ*, 379, 52
- Willott, C., Rawlings, S., Blundell, K., & Lacy, M. 1999, *MNRAS*, 309, 1017
- Willott, C., Rawlings, S., Blundell, K., Lacy, M., & Eales, S. 2001a, *MNRAS*, 322, 536
- Willott, C., Rawlings, S., & Blundell, K. 2001b, *MNRAS*, 324, 1
- Willott, C., Rawlings, S., Jarvis, M., & Blundell, K. 2003, *MNRAS*, 339, 173